Cloud Statistics Measured With the Infrared Cloud Imager (ICI)

Brentha Thurairajah, *Member, IEEE,* and Joseph A. Shaw, *Senior Member, IEEE*

Abstract—The Infrared Cloud Imager (ICI) is a ground-based thermal infrared imaging system that measures spatial cloud statistics with a 320×240-pixel uncooled microbolometer detector array. Clouds are identified from the residual radiance that remains after water vapor emission is removed from radiometrically calibrated sky images (the water vapor correction relies on measurements of precipitable water vapor and near-surface air temperature). Cloud amount, the percentage of an ICI image containing clouds, is presented for data from Atmospheric Radiation Measurement (ARM) sites at Barrow, AK in February–April 2002, Lamont, OK in February–April 2003, and Barrow, AK in March–April 2004. In Oklahoma, the percent cloud cover determined from full ICI images was slightly higher than that found from a single-pixel time series, suggesting that cloudiness may be under sampled by vertically viewing lidars or radars under highly variable conditions. Full-image and single-pixel statistics agreed more closely for Arctic clouds, which tend to be uniform for long periods of time. Good agreement is found in comparing cloud amount from ICI and active remote sensors during day and night, but much worse agreement is found between ICI and the ARM Whole Sky Imager during nighttime relative to daytime, indicating the importance of the diurnally consistent ICI measurements.

Index Terms—Clouds, infrared imaging, infrared radiometry, terrestrial atmosphere.

I. INTRODUCTION

CLOUDS fill an important role in maintaining the radiation budget of the atmosphere by preventing incoming solar radiation from reaching the Earth and outgoing thermal radiation from escaping into space. This radiative impact of clouds, which tend to warm or cool the Earth depending on their optical properties and spatial distribution, is a key component in the global climate [1]. Thus, understanding the spatial distribution and radiative properties of clouds can contribute to improved climate and weather predictions. Spatial cloud distribution also is a key factor in understanding and modeling cloud radiation feedback mechanisms [2].

While satellite sensors achieve global coverage, ground-based sensors provide improved radiometric contrast between clouds and the background. This is especially true at high latitudes, where satellites have difficulty distinguishing between clouds and the underlying surface [3]. Other ground-based cloud measuring instruments generally are either wide-angle, spatially resolving passive imagers or zenith-viewing active sensors. For example, the Total Sky Imager (TSI) [4] measures visible skylight (~ 450–650 nm) from the entire sky dome during daytime, while the Whole Sky Imager (WSI) [5] provides hemispherical coverage with different detection techniques during day and night. The WSI has approximately 70-nm wide imaging bands centered at 450, 650, and 800 nm, identifying clouds from red/blue ratios during the day and from star maps at night (with gaps in operation near sunrise and sunset). More complete diurnal coverage is provided by zenith-viewing active sensors, such as the Micro-Pulse Lidar (MPL) [6] or mm-wave cloud radar (MMCR) [7]. Unless operated in a scanning mode, the active sensors produce spatial cloud statistics by assuming that temporal statistics of clouds at a fixed location are equal to spatial statistics along the direction of the mean wind (Taylor's Hypothesis [8]), which may not hold under conditions such as developing or dissipating clouds [9]. The combination of active sensors and passive imaging sensors may provide enhanced information about the vertical and horizontal cloud distribution, including cloud overlap that can dramatically alter the net radiative impact of the clouds (consider, for example, the difference between two overlapping cloud layers that completely obscure the sun and two nonoverlapping cloud layers that allow direct solar illumination of the surface).

The Infrared Cloud Imager (ICI) is a ground-based passive sensor that measures downwelling atmospheric radiance in the 8–14 μm wavelength band [10]–[14]. ICI data are used with precipitable water vapor and air temperature measurements to identify clouds and calculate cloud amount continuously with no difference in sensitivity during day and night. This system was developed as part of a Japan–U.S. joint venture to study the Arctic atmosphere, led by the Japanese Communications Research Laboratory (CRL, which recently became the National Institute of Information and Communications Technology, www.nict.go.jp). The ICI has been deployed at Poker Flat Research Range (PFRR), Alaska in 2000–2001 [10] and at the Department of Energy's Atmospheric Radiation Measurement (ARM) sites [16] in Barrow, AK in February–April 2002 [10]–[14], Lamont, OK as part of the Cloudiness Intercomparison Campaign from mid February to late April 2003 [10], [15], and again in Barrow, AK for the Arctic Winter Radiometric Experiment in March and April 2004 [10], [17]. Results from Barrow, AK in 2002 and 2004 and Lamont, OK in 2003 are presented here.

B. Thurairajah was with the Electrical and Computer Engineering Department, Montana State University, Bozeman, MT 59717 USA. She is now with the Atmospheric Science program, University of Alaska, Fairbanks, AK 99775 USA.

J. A. Shaw is with the Electrical and Computer Engineering Department, Montana State University, Bozeman, MT 59717 USA (e-mail: jshaw@ece.montana.edu).
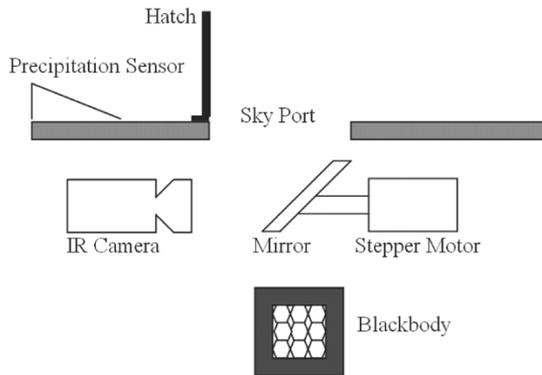
Fig. 1. Block diagram of the ICI optics box. A microbolometer-array infrared camera alternately views blackbody calibration sources and the sky.

II. INSTRUMENT DESCRIPTION

The Infrared Cloud Imager uses an uncooled microbolometer detector array [18] to measure the downwelling atmospheric radiance. The prototype system has a relatively narrow field of view, $18° \times 13.5°$, which has been adequate for demonstrating the capability and developing calibration and data analysis techniques. Because the ICI requires no cryogens or other cooling mechanisms for the detector array, it can be deployed in an unattended mode at remote field sites. The present system has two blackbodies, whereas previous versions had only one blackbody, which reduces both calibration uncertainty and reliance on stability of the instrument housing temperature [10]. Future versions of the ICI will have wide angle imaging capability to obtain cloud cover in a significant fraction of the sky dome.

The primary ICI system components are the infrared camera, two blackbody calibration sources, a gold-plated beam-steering mirror, and control electronics (see Fig. 1). The beam-steering mirror is rotated by a stepper motor to alternately view the blackbodies and the sky, the latter through a sky port that opens when heavy precipitation is not indicated by a precipitation sensor. The optics are housed in an optics box that sits outside, connected via Arctic cables to a computer inside a nearby building or shelter. The system is controlled remotely over a network connection.

The detector is an uncooled microbometer array containing 320×240 pixels, each measuring 50×50 μm. One of the large-area blackbodies floats at the temperature of the optics-box interior (typically ~ 20 °C) and the other is thermo-electrically controlled over a range of 0 °C to 100 °C (typically ~ 50 °C). Prior to the 2004 deployment in Barrow the ICI contained only one blackbody, which was operated at 22.6 °C to monitor the ICI calibration offset; the gain was measured in the laboratory and varied less than 5% as long as the enclosure temperature remained in the range of 15 °C to 20 °C [10]. With the present two-blackbody system, radiometric calibration uncertainty is approximately 2% [10].

The system averages two subsequent images of the blackbody and the sky (a larger number of images can be averaged to reduce noise). Each sky image is calibrated with a linear calibration equation that uses the measured gain and offset to produce radiometric images with units of band-averaged radiance (watts per square meter steradian) [10]. Clouds are identified and classified from the radiance value in each pixel.

III. DATA ANALYSIS

A. Water Vapor Correction

The ICI measures downwelling atmospheric radiance that includes emission from clouds (if present) and atmospheric gases. The magnitude of the downwelling radiance increases with cloud optical thickness and cloud temperature, but also with water vapor content [10]. Other gases that contribute to the ICI radiance include ozone (~ 9.5–10 μm) and carbon dioxide (near the longwave edge of the 8–14-μm ICI band). We do not compensate for ozone directly because its emission is not highly variable in space or time and because ozone is primarily in the stratosphere where it is masked by the lower clouds. On the other hand, CO_2 emission tends to increase the temperature dependence of the clear-sky radiance, so we have incorporated a temperature-dependent water vapor correction that includes the small amount of CO_2 emission that is detected on the longwave edge of the ICI band. This correction and the temperature independent correction used in Barrow are both described in the following paragraphs.

Within the ICI optical bandwidth, water vapor is the most highly variable emission source other than clouds, so we remove the water vapor emission from ICI images to arrive at a residual radiance that is used to identify clouds. The water vapor radiance was determined with the MODTRAN radiative transfer code [19] as a function of precipitable water vapor (PWV = integrated atmospheric column water vapor in cm). Although water vapor is present both above and below clouds, and only that amount below the cloud would contribute to the ICI signal, simulations and experiments both have confirmed that subtracting the entire water vapor emission is a self-correcting problem for cloud detection since high clouds are above essentially all of the water vapor and thick clouds are easy to detect because of their large residual radiance.

For Barrow in winter, we found that the ICI data could be corrected with a fairly simple best-fit line relating band-averaged radiance to PWV without a temperature correction (PWV varied from 0.17 to 1.66 cm in 2002 and from 0.06 to 1.1 cm in 2004, but nearly always remained below 0.5 cm, and air temperature varied from −41 °C to 0 °C). This linear relation was derived from radiative transfer modeling using the standard MODTRAN atmospheric models [20] ranging from cold, dry, Arctic winter to humid tropical conditions to obtain a wide range of PWV values (Fig. 2).

In Oklahoma, however, the atmospheric conditions varied so widely and the humidity was sufficiently high that we found it necessary to incorporate a temperature dependence into the water vapor correction (the air temperature varied from −15 °C to +30 °C and PWV varied over approximately 0.3–3 cm). For this analysis we used the MODTRAN code to calculate four different response curves, each of which expresses integrated radiance as a function of PWV for an atmospheric model with a different near-surface air temperature. One of these curves was calculated for the Tropical atmospheric model, one for the 1976 U.S. Standard atmospheric model, one for the Midlatitude Winter model, and one for the Subarctic Winter atmospheric model [20]. Fig. 3 shows the temperature profiles used in these models, each of which has a corresponding set of profiles of
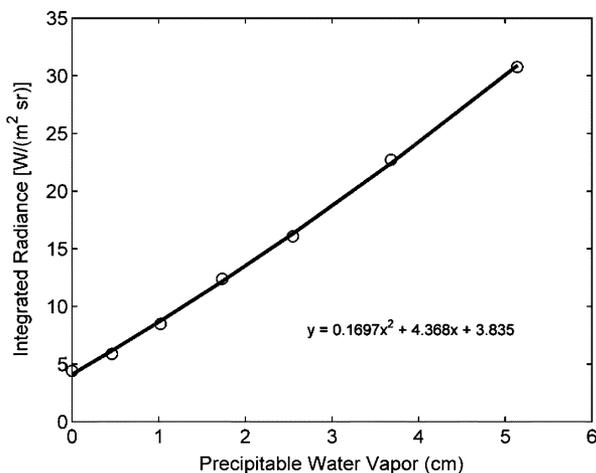
Fig. 2. Band-averaged atmospheric radiance as a function of precipitable water vapor (centimeters) used for removing water vapor emission from Arctic ICI images.

Fig. 4. Temperature-dependent water vapor correction curves used to process Oklahoma ICI data. Each curve is labeled with the near-surface air temperature of the standard Modtran atmospheric model used to calculate radiance versus PWV (see Fig. 3).
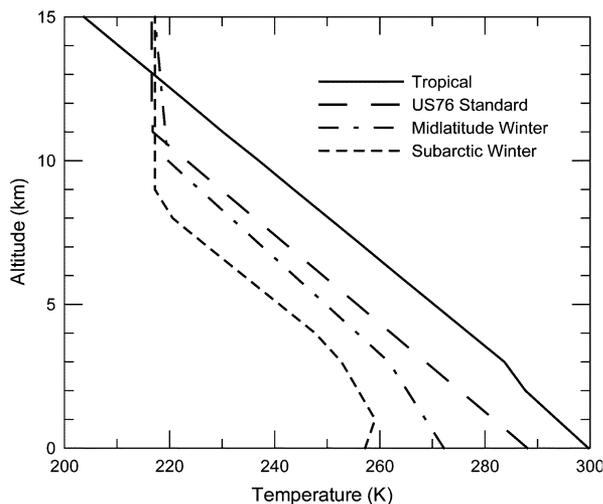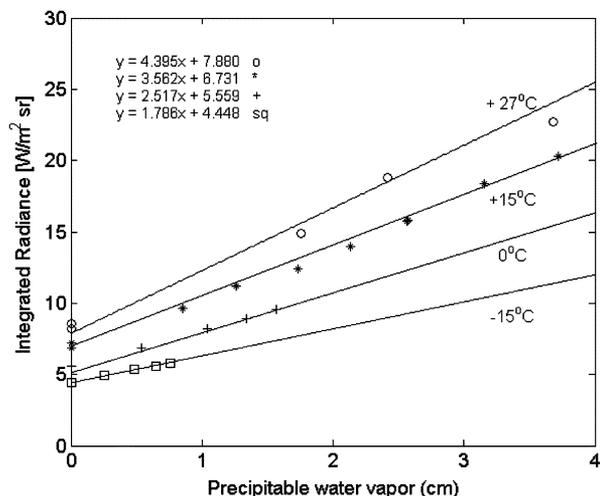

Fig. 3. Atmospheric temperature profiles [20] used in the Modtran calculations for the temperature-dependent water vapor correction. The surface air temperatures for these profiles are approximately $-15\ ^\circ$C, $0\ ^\circ$C, $15\ ^\circ$C, and $27\ ^\circ$C.

water vapor, ozone, carbon dioxide, and all other radiatively significant atmospheric species (because of this the correction also removes the CO_2 emission). While the model profiles do not match the atmospheric state exactly, they provide comparable results to MODTRAN calculations using radiosonde profiles of temperature and water vapor (processed image differences are smaller than the ICI calibration uncertainty of approximately 1–2 W/$(m^2 \cdot sr)$ [10]). These curves allow ICI images to be processed without relying on infrequent radiosonde profiles.

Fig. 4 shows the temperature-dependent water vapor correction curves, each of which was generated by varying the PWV in the corresponding MODTRAN atmospheric model (for which the temperature profile is shown in Fig. 3). Each response curve in Fig. 4 is characterized according to the near-surface air temperature in the corresponding temperature profile ($-15\ ^\circ$C, $0\ ^\circ$C, $+15\ ^\circ$C, and $+27\ ^\circ$C). The magnitude of the water vapor correction applied to each ICI image is determined by the

value of PWV measured by a nearby microwave radiometer (MWR) and the value of the 2-m air temperature from the Surface Meteorological Observation System (SMOS; data for both the MWR and SMOS were obtained from the ARM data archive, www.arm.gov/data/). So, for example, an ICI image acquired with a near-surface air temperature of $27\ ^\circ$C would be corrected by the amount found from the top curve in Fig. 4 for the measured value of PWV. A linear interpolation between the two nearest response curves is used when the near-surface air temperature is between two curves.

It is important to recognize that the near-surface air temperature is used only to choose which atmospheric model is closest to the actual conditions for each image; it is not used in place of the cloud temperature or as the temperature of the air between the ICI and the cloud. Full, detailed profiles of air temperature, water vapor, and other gases were used in each MODTRAN atmospheric model [20] to calculate the band-integrated downwelling radiance as a function of PWV, resulting in the curves in Fig. 4 (note also that a least squares fit through all the data points in Fig. 4 reproduces the single curve in Fig. 2). Atmospheric emission also increases with zenith angle, so an angle-dependent water vapor correction will be required in future wide-angle systems. However, for the limited angular field of the current system, neglecting this leads to an error of only 0.25 W/$(m^2 \cdot sr)$ at the image edge.

The effectiveness of the water vapor correction is best illustrated with an example. Fig. 5 shows ICI images from Oklahoma with air temperature $= 17\ ^\circ$C and PWV $= 1.3$ cm before (top) and after (bottom) application of the temperature-dependent water vapor correction. Both images are color coded in units of band-average radiance. In these images the sky is mostly clear on the left-hand side and cloudy on the right-hand side, with brightness temperatures of approximately $-40\ ^\circ$C and $0\ ^\circ$C, respectively (Arctic winter clear-sky brightness temperature often is near $-80\ ^\circ$C). The clear (dark blue) regions in the water-vapor-corrected image [Fig. 5(b)] have residual radiance less than 2 W/$(m^2\ sr)$, which is sufficiently
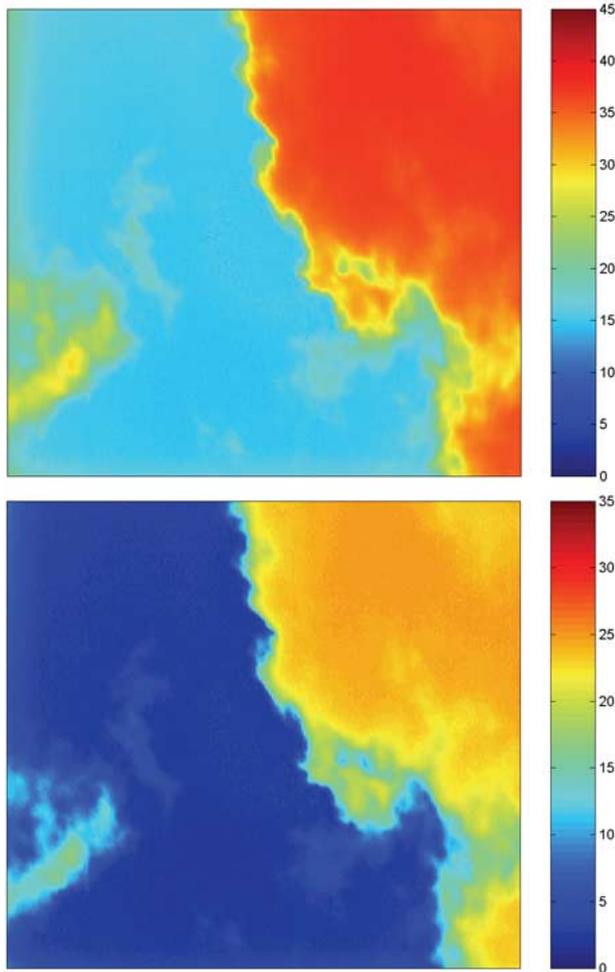
Fig. 5.   ICI images (top) before and (bottom) after the temperature-dependent water vapor correction (note the different scales). The images are from Oklahoma on April 20, 2003, with air temperature = 17 °C and PWV = 1.3 cm. The clear-sky region in the bottom image has residual radiance less than 2 W/(m² · sr), below the default cloud threshold of 2.65 W/(m² · sr), indicating successful removal of noncloud atmospheric emission.

less than the default Oklahoma cloud threshold of 2.65 (described in Section III-B) to be classified as clear. The residual radiance is ~ 25 W/(m² · sr) for the bright cloud on the right-hand side, 15 W/(m² · sr) for the small patch at lower left, and 4.5 W/(m² · sr) for the wispy patch between the two brighter clouds. Therefore, Fig. 5 demonstrates that the water vapor correction is effective at separating cloudy and clear pixels, even in a region between clouds (which may not be as clear as a truly clear sky). Many clear images have residual radiance smaller than 1 W/(m² · sr), especially in recent ICI data with the more stable calibration [10]. A wider variety of images and movies from the ICI can be seen elsewhere [10].

B. Cloud Thresholds

Following water vapor correction, the residual radiance is used to identify and classify clouds. Clouds are identified in pixels where the residual radiance is greater than a threshold value. The first threshold was determined, by considering the radiometric calibration uncertainty, ICI system stability, and water vapor retrieval uncertainty, to be 1.5 W/(m² · sr), after

which comparisons with other sensors were used to refine the threshold. For example, we compared ICI data from varying sky conditions with the Actively Remotely Sensed Cloud Locations (ARSCL) value-added product, which is a data product generated from a combination of lidar, radar, and radiometer data at the ARM measurement sites in a manner designed to produce optimal cloud detection that avoids limitations of each individual sensor [21]. Our objective was not to force the ICI to reproduce the ARSCL data exactly, but rather to identify periods when the ICI measured either significantly less or significantly more clouds. We used data from a variety of ARM sensors for these periods to determine if the ICI was seeing real clouds not detected by other sensors or if the ICI was missing real clouds that were detected by other sensors. In this way, the best cloud-identification threshold was determined to be 1.5 W/(m² · sr) for Barrow data and 2.65 W/(m² · sr) for Oklahoma data.

Sometimes with a constant threshold the ICI identifies thick haze, fog, or aerosols as clouds, and at other times it misses thin cirrus clouds. Therefore, we have begun using an adaptive threshold (explained later) that allows a higher value to greatly reduce incidences of identifying haze as clouds and a lower value to increase sensitivity to thin cirrus. In Section IV, we show results obtained with a constant threshold for Barrow data and an adaptive threshold for the Oklahoma data.

IV. ICI CLOUD MEASUREMENTS

The first-order statistical cloud property of interest in radiative transfer and climate models is the percent cloud cover, which is referred to here as cloud amount to distinguish it from cloud fraction, which usually is expressed as a function of altitude. Images from the prototype ICI system are of sufficiently narrow angular coverage that they accurately represent the horizontal cloud cover in that portion of the sky; however, to avoid biasing the cloud amount with cloud sides, future wide-angle versions of the ICI will be designed with a field of view near 100° (zenith ±50°), which has been shown by Kassianov et al. [22] to provide optimal correlation between cloud amount measured from a hemispherical imager and the quantity needed by modelers.

Using the data analysis methods described in the previous section, we computed monthly and weekly cloud amount for data from the Barrow 2002, Oklahoma 2003, and Barrow 2004 deployments. Fig. 6 shows histograms of monthly ICI cloud amount, determined as the fractional number of cloudy images (we recorded one image per 10 min in Barrow 2002 and one image per minute in Oklahoma 2003 and Barrow 2004). In other words, the figure shows the number of pixels that have a residual radiance greater than 1.5 W/(m² · sr) for Barrow and 2.65 W/(m² · sr) for Oklahoma, divided by the total number of pixels in an image, plotted in 10% bins.

The monthly statistics for Barrow show that the rate of occurrence for 90% to 100% cloudiness was 39% in March 2002, 65% in April 2002, 38% in March 2004, and 42% in the first nine days of April 2004. In a study of Arctic cloud characteristics during the 1997–1998 SHEBA project Intrieri et al. [23] analyzed cloud zenith-viewing cloud radar and lidar data to determine that the monthly-average cloud occurrence increased from
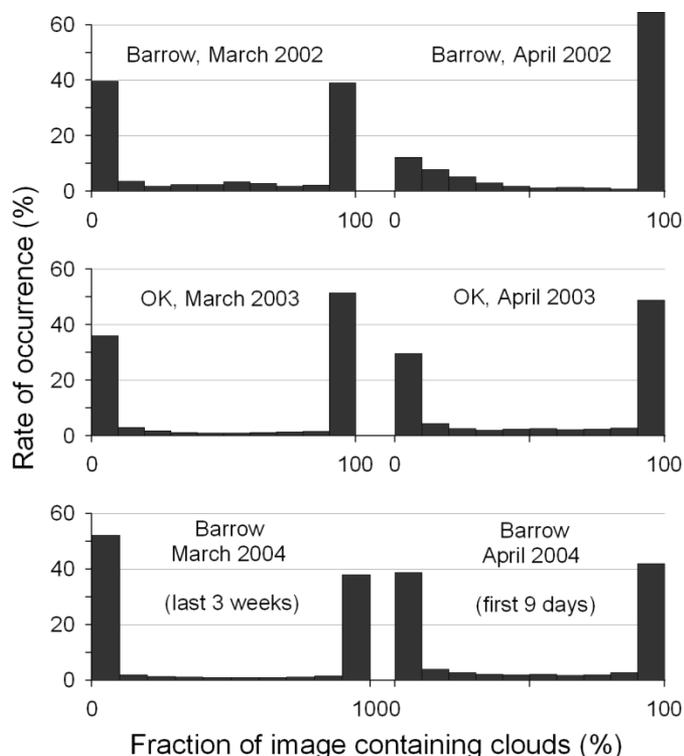
Fig. 6. Monthly cloud cover statistics derived from ICI data for (top) Barrow, AK 2002, (middle) Lamont, OK 2003, and (bottom) Barrow, AK 2004.
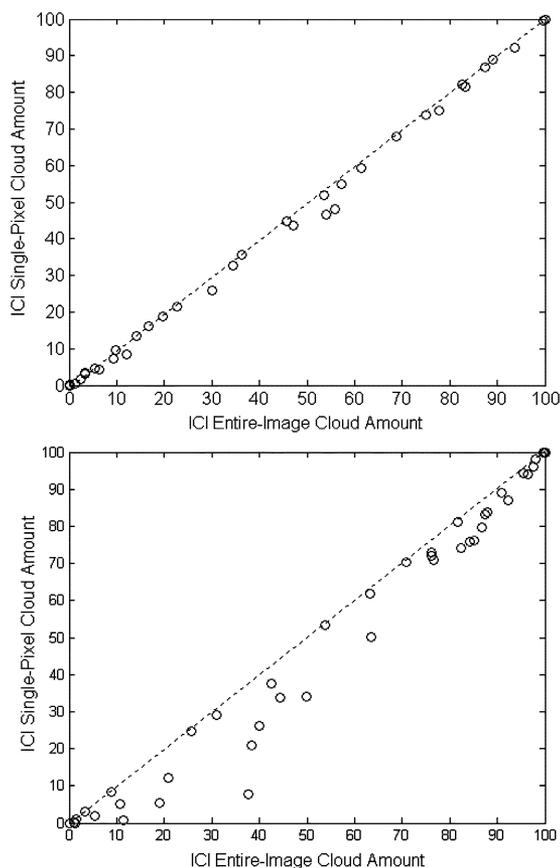

Fig. 7. Scatter plots of single-pixel and full-image ICI cloud statistics from (top) Alaska 2004 and (bottom) Oklahoma 2003. The single pixel predicts slightly less cloudiness than the full image for the Oklahoma data, but this effect is nearly absent in the Alaska data.

80% in March to almost 90% in April. The results from ICI show a similar trend in increasing cloudiness, but with lower values that may be a result of the different locations, the ICI being deployed in Barrow (coastal) and the SHEBA measurements being taken further north on the Arctic Ocean pack ice. Although the ICI data in March 2002 are limited to only about half a month because of the unavailability of MWR water vapor data, we have a continuous record from March 2004 with one image each minute. The bimodal nature of cloudiness at Barrow (clear or overcast) is typical of what has been observed by Intrieri *et al.* [23] and other previous investigators, and suggests that perhaps wide-angle imaging may not be so critically needed in the Arctic.

The overall monthly statistics from Oklahoma depict a similar trend toward mostly clear or mostly cloudy skies, with approximately 40% cloudiness in both March and April 2003. The monthly frequency of sky cover derived from the broadband shortwave radiometers used at the SGP ARM site show that over a period of six years from 1996 to 2001, the monthly cloudiness varied from 25% to 45% for both March and April and the trend of seeing mostly clear and/or cloudy skies is similar to what is seen by the ICI [24].

Beyond just measuring cloudiness, one of the questions we set out to explore with the ICI measurements is whether there are significant differences in cloud amount measured by zenith-viewing and imaging sensors. Statistics determined from zenith sensors are assumed equal to spatial statistics through Taylor's hypothesis, which states that the covariance in time is related to the covariance in space by the speed of the mean flow when the turbulence is small compared to the mean flow [8]; however, Sun and Thorne [9] indicated that this assumption may

break down with dissipating or developing clouds, multilayered clouds, or when the wind speed and direction are changing. Although the ICI determines spatial statistics directly from the measured radiance without invoking Taylor's hypothesis, it is difficult to say much about the difference between temporal and spatial statistics by comparing data from different sensors because of the differing instrument sensitivities, thresholds, and retrieval techniques. Therefore, to address this question without relying on a comparison of data from different sensors, we compared statistics calculated from a single ICI pixel to statistics calculated from full ICI images. Cloud statistics were calculated from the single-pixel radiance time series as the percentage of samples for which that pixel's residual radiance exceeded the cloud threshold. The same analysis was applied also to each full image, but the average cloud amount (CA) in percent was determined for N images as

$$\text{CA} = \frac{100}{N} \sum_{n=1}^{N} \left(\frac{\sum \# \text{ cloudy pixels per image}}{\text{total } \# \text{ of pixels per image}} \right). \quad (1)$$

Fig. 7 shows scatter plots of the single-pixel and full-image ICI cloud amount data from Barrow 2004 and Oklahoma 2003. These plots show that single-pixel measurements slightly underestimate cloudiness relative to the full ICI images in Oklahoma. However, in the Barrow 2004 data the single-pixel and full-image cloud amounts are very nearly equal except on just a few days. The Barrow 2004 experiment was characterized by
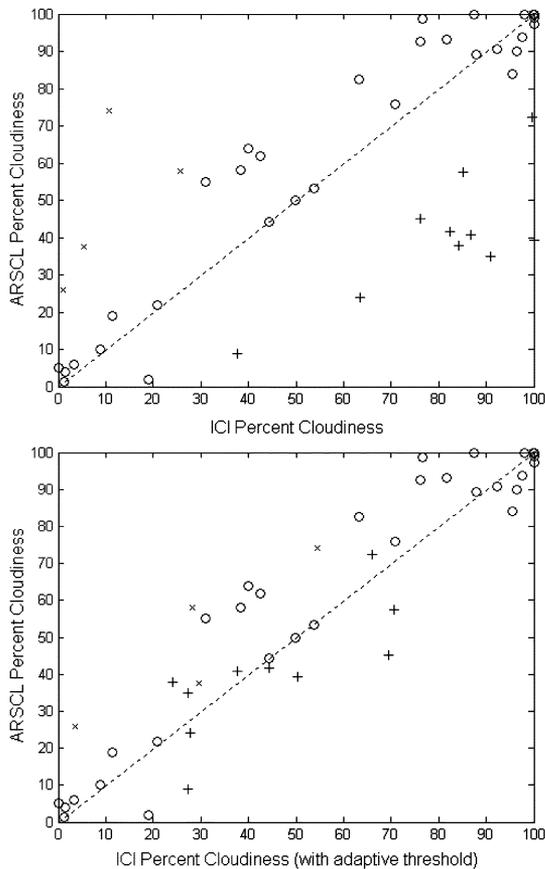
Fig. 8. Scatter plots of MPL and ICI daily cloud amount (top) with a constant ICI threshold and (bottom) with an adaptive ICI threshold to increase cirrus sensitivity and decrease haze sensitivity. The symbols indicate days for which the adaptive threshold algorithm identified significant haze (+), cirrus (×), or neither (○).

particularly persistent periods of clear or overcast skies (multiple hours to days); however, the clouds were more variable on the few days when the cloud amount was noticeably less for the single pixel than for the full images. Several of these days included highly variable cirrus, and the others had broken low clouds with intermittent clear periods. The Alaska 2004 data (top) have correlation coefficient of 0.999 (between the ICI full-image and single-pixel cloud amounts) and rms difference of 1.56, while the Oklahoma 2003 data have correlation coefficient of 0.988 and rms difference of 7.69.

In accordance with the expectation that Taylor's hypothesis applies best to clouds that are not rapidly changing, the single-pixel and full-image data agree most closely during the dominant periods of steady clear or overcast conditions in the Alaska 2004 experiment, but disagree more often (and by a larger amount) for the Oklahoma 2003 experiment, which experienced dramatically higher cloud variability. Given the modest field of view of the prototype ICI system, this analysis does not exactly represent the difference between zenith and full-sky imager data, but does suggest that there may be measurable differences in cloud cover statistics derived from zenith and imaging sensors with variable clouds. Establishing this more fully will require analysis of a longer dataset.

The need for the adaptive cloud-identification threshold mentioned earlier is illustrated in Fig. 8. The top scatter plot

shows MicroPulse Lidar (MPL) and ICI daily cloud amount from March and April 2003 in Oklahoma, with a constant $2.65 \text{ W}/(\text{m}^2 \cdot \text{sr})$ ICI threshold. Although there is reasonable agreement between the two sensors (correlation = 0.752, rms = 24.5), sometimes the ICI constant threshold detects haze as cloud and fails to detect thin cirrus clouds. For the data shown in Fig. 8 we relied primarily on cloud lidar data to trigger the adaptive threshold because of the lidar's high sensitivity to both cirrus and haze, although another useful cloud indicator is the variance of a broadband solar irradiance time series. The current adaptive threshold algorithm checks for the presence of cirrus and low-level haze in an MPL time series during a variable-length running time window (typically several hours to a day). If cirrus is present and low-level haze is not, the ICI threshold is reduced to a lower value, found to be optimal at $1.5 \text{ W}/(\text{m}^2 \cdot \text{sr})$. Low-level haze is detected in the MPL data by examining the strength of the lidar backscatter in the bottom 500 m. If the logarithm of this low-level MPL backscatter power exceeds 4.5, the algorithm increases the ICI threshold to at least $3.5 \text{ W}/(\text{m}^2 \cdot \text{sr})$, with higher thresholds for much stronger low-level lidar signals (not exceeding $6 \text{ W}/(\text{m}^2 \cdot \text{sr})$). This algorithm will miss thin cirrus during periods of thick low-level haze, but will not miss low-level clouds because even with a higher threshold such clouds are nearly impossible to miss because of their large residual radiance.

The bottom scatter plot in Fig. 8 shows the same data as the top plot, but with the adaptive ICI threshold. The × symbols indicate days on which the constant threshold missed cirrus clouds that were seen consistently in MPL data, while the + symbols indicate days on which the constant threshold classified low-level haze as clouds (haze is indicated by high relative humidity and near-surface MPL backscatter). The adaptive threshold results in correlation = 0.937 and rms = 12.45 (although these adaptive threshold results are a result of postexperiment data processing, the procedure can be automated as long as the ancillary data streams are available). Research is continuing into improved adaptive algorithms, including using aerosol size distributions and scattering coefficients to help identify periods of low-level haze.

We also investigated the day-night consistency of ICI cloud statistics (Fig. 9). Since the ICI measures thermal emission, its cloud sensitivity and retrieval accuracy are not expected to vary significantly over a diurnal cycle. A key tradeoff in ground-based measurement of cloud statistics has been that zenith-viewing active sensors (e.g., radars and lidars) provide vertically resolved measurements with high consistency over a diurnal cycle, but do not provide information about clouds away from the zenith when not scanning. Conversely, imaging sensors provide horizontal spatial information, but have difficulty doing so consistently during both day and night. Some imaging sensors (e.g., TSI) provide daytime data only, while others (e.g., WSI) measure daytime and nighttime data with different spatial resolution, bandwidth, and retrieval technique (red-blue ratios in day and star maps at night).

In Fig. 9 we show scatter plots of cloud data from the ARSCL cloud product [21] and ICI for daytime (top) and nighttime (bottom). The lack of a significant day-night difference provides evidence of the ICI's consistency over a diurnal cycle (the ARSCL active sensors have essentially constant daytime and nighttime sensitivity). The daytime scatter plot has a correlation
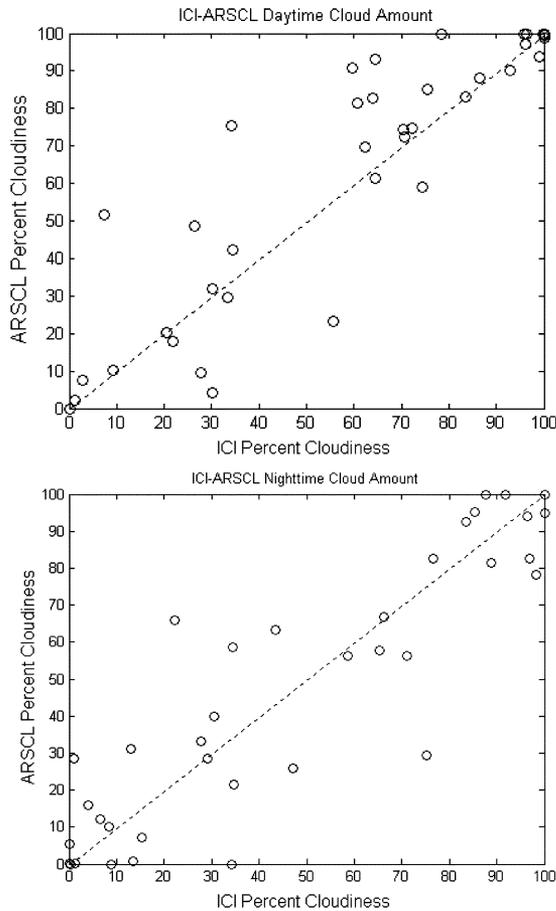
Fig. 9. Scatter plots of ARSCL and ICI cloud amount for (top) daytime, with correlation coefficient = 0.90 and rms difference = 15.7 and (bottom) nighttime, with correlation coefficient = 0.90 and rms difference = 15.9.
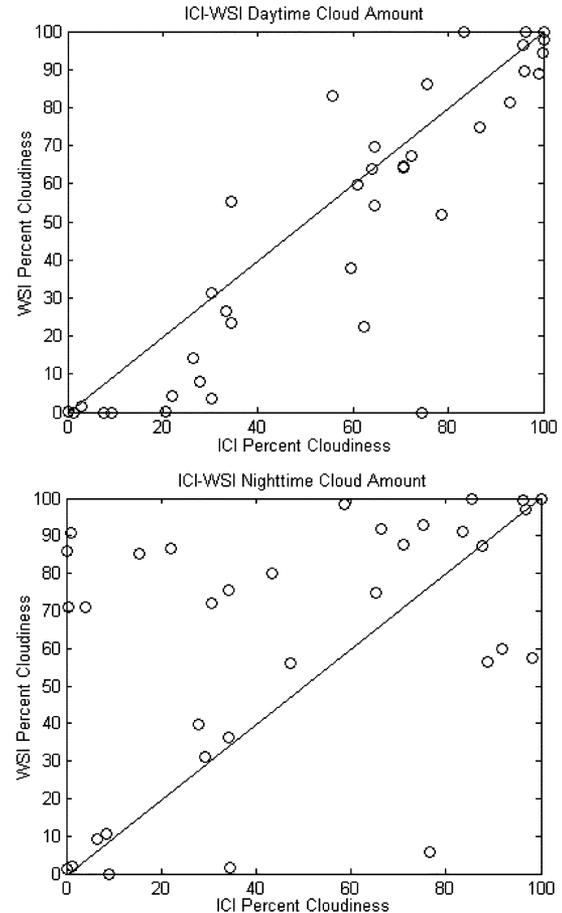

Fig. 10. Scatter plots of WSI and ICI cloud amount for (top) daytime, with correlation coefficient = 0.90 and rms difference = 18.0 and (bottom) nighttime, with correlation coefficient = 0.52 and rms difference = 37.5.

coefficient = 0.90 between ARSCL and ICI with rms difference = 15.7; the nighttime data have correlation coefficient = 0.90 between ARSCL and ICI, with rms difference = 15.9.

A much different comparison is shown in Fig. 10, which compares WSI and ICI data during daytime (top) and nighttime (bottom). Whereas the WSI daytime data agree reasonably well with the ICI data (correlation = 0.90 between ICI and WSI percent cloudiness, rms = 17.95), the WSI nighttime data derived from star maps significantly overestimate cloudiness relative to the ICI (correlation = 0.52 between ICI and WSI percent cloudiness, rms = 37.53). These results of data from several months of deployment suggest that the ICI is capable of providing a continuous and consistent data stream of spatial cloud statistics that can be used to study the diurnal radiative impact of clouds.

V. CONCLUSION

The Infrared Cloud Imager has been deployed successfully in the widely varying environmental conditions of Alaska and Oklahoma (in addition to substantial testing between deployments in both Colorado and Montana). Cloud statistics presented here from Barrow, Alaska in 2002 and 2004 and Lamont, Oklahoma in 2003 agree well with cloud lidar data when an adaptive threshold is used on the Oklahoma ICI data. The ICI data have been used to demonstrate that a small bias occurs between zenith-viewing and sky-imaging cloud sensors with variably

scattered clouds, with the zenith-viewing sensors slightly underestimating cloudiness relative to imaging sensors. Much larger biases occur when different retrieval techniques are used to derive cloud statistics during day and night. Future work on the ICI technique will focus on developing a wide-angle system and demonstrating even more robust adaptive-threshold algorithms. Studying diurnal cloud variability and the variation in cloud characteristics near sunrise and sunset, when other instruments have problems measuring clouds, may give us important results that can be used in cloud models. In addition to weather and climate studies, the ICI system can be used to measure spatially resolved cloud statistics for use in determining link-availability statistics for Earth-space optical communications.

ACKNOWLEDGMENT

REFERENCES

[1] V. Ramanathan, B. Subasilar, G. J. Zhang, W. Conant, R. D. Cess, J. T. Keihl, H. Grassl, and L. Shi, "Warm pool heat budget and shortwave cloud forcing: A missing physics?," *Science*, vol. 267, pp. 499–503, Jan. 1995.

[2] J. A. Curry, W. B. Rossow, D. Randall, and J. L. Shramm, "Overview of arctic cloud and radiation characteristics," *J. Clim.*, vol. 9, pp. 1731–1764, Aug. 1996.

[3] Z. Li, M. C. Cribb, F.-L. Chang, and A. P. Trischenko, "Validation of MODIS-retrieved cloud fractions using whole sky imager measurements at the three ARM sites," presented at the *14th Atmospheric Radiation Measurement (ARM) Science Team Meeting*, Albuquerque, NM, Mar. 2004. [Online]. Available: http://www.arm.gov/publications/proceedings/conf14/extended_abs/li1-z.pdf.

[4] C. N. Long, D. W. Slater, and T. Tooman. Total Sky Imager Model 880 status and testing results. U.S. Dept. Energy, Washington, DC. [Online]. Available: http://www.arm.gov/publications/tech_reports/arm-tr-006.pdf.

[5] T. P. Tooman. Whole Sky Imager retrieval guide. U.S. Dept. Energy, Washington, DC. [Online]. Available: http://www.arm.gov/publications/tech_reports/arm-tr-011-1.pdf.

[6] J. R. Campbell, D. L. Hlavka, E. J. Welton, C. J. Flynn, D. D. Turner, J. D. Spinhirne, V. S. Scott, and I. H. Hwang, "Full-time, eye-safe cloud and aerosol lidar observation at atmospheric radiation measurement program sites: Instrument and data processing," *J. Atmos. Oceanic Technol.*, vol. 19, pp. 431–442, 2002.

[7] E. E. Clothiaux, K. P. Moran, B. E. Martner, T. P. Ackerman, G. G. Mace, T. Uttal, J. H. Mather, K. B. Widener, M. A. Miller, and D. J. Rodriguez, "The atmospheric radiation measurement program cloud radars: Operational modes," *J. Atmos. Sci.*, vol. 56, pp. 819–827, 1999.

[8] G. Kunz, "Field testing of a lidar wind profiler," *Opt. Eng.*, vol. 35, pp. 3074–3083, 1996.

[9] C. H. Sun and L. P. Thorne, "Inferring spatial cloud statistics from limited field of view zenith observations," presented at the *5th ARM Science Team Meeting, CONF—9503140*, San Diego, CA, Mar. 1995. [Online]. Available: http://www.arm.gov/publications/proceedings/conf05/abstracts/76_95.pdf.

[10] J. A. Shaw, P. W. Nugent, N. Pust, B. Thurairajah, and K. Mizutani, "Radiometric cloud imaging with an uncooled microbolometer thermal infrared camera," *Opt. Express*, vol. 13, 2005.

[11] B. Thurairajah, "Thermal infrared imaging of the atmosphere: The Infrared Cloud Imager," M.S. thesis, Elect. Comput. Eng. Dept., Montana State Univ., Bozeman, 2004.

[12] J. A. Shaw, B. Thurairajah, E. Edqvist, and K. Mizutani, "Infrared cloud imager deployment at the north slope of Alaska during early 2002," presented at the *12th ARM Science Team Meeting, CONF-2002*, St. Petersburg, FL, Apr. 2002. [Online]. Available: http://www.arm.gov/publications/proceedings/conf12/extended_abs/shaw-ja.pdf.

[13] J. A. Shaw and B. Thurairajah, "Short-term arctic cloud statistics at NSA from the infrared cloud imager," presented at the *13th ARM Science Team Meeting*, Broomfield, CO, Apr. 2003. [Online]. Available: http://www.arm.gov/publications/proceedings/conf13/extended_abs/shaw-ja.pdf.

[14] J. A. Shaw and B. Thurairajah, "Statistics of Alaskan clouds from the infrared cloud imager (ICI)," in *Proc. SPIE Conf. Optical Spectroscopic Techniques and Instrumentation for Atmospheric and Space Research V*, vol. 5157, San Diego, CA, 2003, pp. 1–6.

[15] B. Thurairajah and J. A. Shaw, "Infrared cloud imager measurements of cloud statistics from the 2003 cloudiness intercomparison campaign," presented at the *14th Atmospheric Radiation Measurement (ARM) Science Team Meeting*, Albuquerque, NM, Mar. 2004. [Online]. Available: http://www.arm.gov/publications/proceedings/conf14/extended_abs/thurairajah-b.pdf.

[16] T. P. Ackerman and G. Stokes, "The atmospheric radiation measurement program," *Phys. Today*, vol. 56, pp. 38–45, 2003.

[17] E. R. Westwater, M. Klein, V. Leuski, A. J. Gasiewski, T. Uttal, D. A. Hazen, D. Cimini, V. Mattioli, B. L. Weber, S. Dowlatshahi, J. A. Shaw, J. C. Liljegren, B. M. Lesht, and B. D. Zak, "The 2004 north slope of Alaska Arctic winter radiometric experiment," presented at the *14th ARM Science Team Meeting*, Albuquerque, NM, Mar. 2004. [Online]. Available: http://www.arm.gov/publications/proceedings/conf14/extended_abs/westwater-er.pdf.

[18] P. W. Kruse, *Uncooled Thermal Imaging: Arrays, Systems, and Applications*. Bellingham, Washington: SPIE Press, 2001, vol. TT-51, ch. 1 and 4.

[19] J. Wang, G. P. Anderson, H. E. Revercomb, and R. O. Knuteson, "Validation of Fascode and Modtran3: Comparison of model calculations with ground-based and airborne interferometer observations under clear-sky conditions," *Appl. Opt.*, vol. 35, pp. 6028–6040, Oct. 1996.

[20] G. P. Anderson, S. A. Clough, F. X. Kneizys, J. H. Chetwynd, and E. P. Shettle, "AFGL atmospheric constituent profiles," Air Force Geophys. Lab., Hanscom AFB, MA, Rep. AFGL-TR-86-0110, 1986.

[21] E. E. Clothiaux, T. P. Ackerman, G. G. Mace, K. P. Moran, R. T. Marchand, M. Miller, and B. E. Martner, "Objective determination of cloud heights and radar reflectivities using a combination of active remote sensors at the ARM CART sites," *J. Appl. Meteorol.*, vol. 39, pp. 645–665, 2000.

[22] E. I. Kassianov, C. N. Long, and M. Ovtchinnikov, "ARM total sky imager: Monte Carlo simulations," presented at the *12th ARM Science Team Meeting*, St. Petersburg, FL, Mar. 2002. [Online]. Available: http://www.arm.gov/publications/proceedings/conf12/extended_abs/kassianov1-ei.pdf.

[23] J. M. Intrieri, M. D. Shupe, T. Uttal, and B. J. McCarty, "An annual cycle of arctic cloud characteristics observed by radar and lidar at SHEBA," *J. Geophys. Res.—Oceans*, vol. 107, pp. 5-1–5-15, Oct. 2002.

[24] K. L. Gaustad and C. N. Long, "An evaluation of cloud cover, cloud effect, and surface radiation budgets at the SGP and TWP ARM sites," in *12th ARM Science Team Meeting*, St. Petersburg, FL, Apr. 2002. [Online]. Available: http://www.arm.gov/publications/proceedings/conf12/extended_abs/gaustad-kl.pdf.

Brentha Thurairajah (M'04) was born in Jaffna, Sri Lanka. She received the B.E. degree in electronics and communication engineering from the University of Madras, Madras, India, and the M.S. degree in electrical engineering from Montana State University, Bozeman, in 2001 and 2004, respectively. She is currently pursuing the Ph.D. degree at the University of Alaska, Fairbanks.

Joseph A. Shaw (S'84–M'90–SM'04) was born in Bozeman, MT. He received the B.S. degree in electrical engineering from the University of Alaska, Fairbanks, the M.S. degree in electrical engineering from the University of Utah, Salt Lake City, and the M.S. and Ph.D. degrees in optical sciences from the University of Arizona, Tucson, in 1987, 1989, 1994, and 1996, respectively.

He was an Electro-optical Engineer at the National Oceanic and Atmospheric Administration (NOAA) Environmental Technology Laboratory, Boulder, CO, from 1989 to 2001, where he developed infrared spectroradiometers and laser sensors for studying the Earth's atmosphere and oceans. In 2001, he became Associate Professor of electrical and computer engineering at Montana State University, Bozeman. His current research is in polarimetric and radiometric imaging and laser remote sensing.

Dr. Shaw is a Fellow of the OSA and a member of SPIE. For his contributions to optical remote sensing science, engineering, and education, he received a Presidential Early Career Award for Scientists and Engineers, the international Vaisala Award from the World Meteorological Organization, a NOAA Bronze Medal Award, and a NOAA Outstanding Scientific Paper Award.